

JGR Space Physics

RESEARCH ARTICLE

10.1029/2021JA029322

Key Points:

- Intense unguided mode electromagnetic ion cyclotron waves have been identified in the radiation belt
- Protons with a few hundred keV provide the free energy for the growth of unguided L-mode waves
- Spatial inhomogeneity of ion abundance ratios controls the potential trapping of unguided waves

Supporting Information:

Supporting Information may be found in the online version of this article.

Correspondence to:

G. Wang, and T. Zhang,
wanggengayst@163.com;
tiealong.zhang@oeaw.ac.at

Citation:

Wang, G., Gao, Z., Wu, M., Wang, G., Xiao, S., Chen, Y., et al. (2021). Trapping and amplification of unguided mode EMIC waves in the radiation belt. *Journal of Geophysical Research: Space Physics*, 126, e2021JA029322. <https://doi.org/10.1029/2021JA029322>

Received 8 MAR 2021

Accepted 7 AUG 2021

Trapping and Amplification of Unguided Mode EMIC Waves in the Radiation Belt

Geng Wang¹ , ZhongLei Gao^{2,3} , MingYu Wu¹ , GuoQiang Wang¹ , SuDong Xiao¹, YuanQiang Chen³ , ZhengYang Zou⁴, and TieLong Zhang^{1,5} 

¹Harbin Institute of Technology, Shenzhen, China, ²School of Physics and Electronic Sciences, Changsha University of Science and Technology, Changsha, China, ³Key Laboratory of Geospace Environment, University of Science and Technology of China, Chinese Academy of Sciences, Hefei, China, ⁴State Key Laboratory of Lunar and Planetary Sciences, Macau University of Science and Technology, Macao, China, ⁵Space Research Institute, Austrian Academy of Sciences, Graz, Austria

Abstract Electromagnetic ion cyclotron (EMIC) waves can cause the scattering loss of the relativistic electrons in the radiation belt. They can be classified into the guided mode and the unguided mode, according to wave's propagation behavior. The guided mode waves have been widely investigated in the radiation belt, but the observation of the unguided mode waves have not been expected. Based on the observations of Van Allen Probes, we demonstrate for the first time the existence of the intense unguided L-mode EMIC waves in the radiation belt according to the polarization characteristics. Growth rate analyses indicate that the hot protons with energies of a few hundred keV may provide the free energy for wave growth. The reflection interface formed by the spatial locations of local helium cutoff frequencies can be nearly parallel to the equatorial plane when the proton abundance ratio decreases sharply with *L*-shell. This structure combined with hot protons may lead to the trapping and significant amplification of the unguided mode waves. These results may help to understand the nature of EMIC waves and their dynamics in the radiation belt.

Plain Language Summary Electromagnetic ion cyclotron (EMIC) waves play an important role in the radiation belt. They can be classified into the guided mode and the unguided mode, according to wave's propagation behavior. Based on the observations of Van Allen Probes, we demonstrate for the first time the existence of the intense unguided mode EMIC waves in the radiation belt. Their energy comes from the hot protons with energies of a few hundred keV. As the spatial variation of ion abundance ratios could form a trapping region, where the unguided mode waves can be amplified significantly. These results may help to understand the nature of EMIC waves and their dynamics in the radiation belt.

1. Introduction

Earth's radiation belt is dynamically influenced by multiple types of waves, one of them is the electromagnetic ion cyclotron (EMIC) wave, which has been widely investigated in recent decades (e.g., Kasahara et al., 1992; Keika et al., 2013; Tetrck et al., 2017; D. Wang et al., 2015; Wang, Huang, et al., 2017, and others). EMIC waves have often been observed just below the hydrogen (H^+) gyrofrequencies (f_{cH^+}), with left-hand polarizations (L-mode) and quasi-parallel wave vectors (Meredith et al., 2014; Saikin et al., 2015; Wang, Huang, et al., 2017). In the radiation belt, the existence of minor ions (He^+ and O^+) separates the cold plasma dispersion curves of EMIC waves into several branches, and the L-mode EMIC waves can belong to two types of propagation modes: one is the guided mode and the other is the unguided mode (Figure S1), according to whether the wave group velocity is guided by the ambient magnetic field (Rauch & Roux, 1982).

The guided mode waves can propagate in the same *L*-shell within which the substorm injected hot ions are trapped. The anisotropic hot H^+ with the energy of tens of keV can resonate with the waves of guided mode, and lead to the wave growth (e.g., Anderson & Hamilton, 1993; Cornwall, 1965; Yu et al., 2016, and others). The anisotropy of hot ions has largest value at local minima of magnetic field and decreases with latitude (Cornwall, 1965), accounting for the equatorial confinement ($\leq 11^\circ$) of the observed source region (Loto'Aniu et al., 2005). Normally, higher wave growth favors the more field aligned wave vector (Horne & Thorne, 1993), as supported by (D.-Y. Lee et al., 2018; Saikin et al., 2015). For the guided waves, the wave

vectors should quickly turn oblique where the refractive indexes are larger, as a consequence of Snell's law, as demonstrated by simulations (Horne & Thorne, 1993) and observations (Yue et al., 2019). In the vicinity of plasmapause, the tendency of turning oblique can be counteracted by negative density gradient (Horne & Thorne, 1993), which facilitates the wave growth (Chen et al., 2009; de Soria-Santacruz et al., 2013), although the effect is limited (Fraser & Nguyen, 2001; Halford et al., 2015; Tetrack et al., 2017). At approximately $10^\circ - 20^\circ$ (Jun et al., 2019), poleward waves should approach the local bi-ion frequencies (Rauch & Roux, 1982), where the wave energy could be reflected (Khazanov et al., 2006), absorbed by heavy ions (Horne & Throne, 1997; Thorne & Horne, 1993) or transmitted (Hu et al., 2010), depending on the abundance ratios of heavy ions (Hu et al., 2010).

Refractive index distribution is approximately isotropic for unguided mode waves (Rauch & Roux, 1982), therefore the group velocity should follow the wave vector and not be guided by the magnetic field. As the wave vector and Poynting flux could turn oblique very quickly, the unguided mode waves are likely to propagate to larger L -shell rapidly (Horne & Thorne, 1993). Kim and Johnson (2016) performed 2-D full-wave simulation and found that the unguided waves propagate to the stronger magnetic field can be reflected at cutoff frequency and propagate to the outer magnetosphere. Moreover, as the wavenumber of the unguided mode is relatively larger than that of the guided mode (Figure S1), the resonant energy may exceed the peak energy of the substorm injected hot H^+ , which does not favor the wave generation. Therefore, it is supposed that the inner magnetosphere does not support the amplification of intense unguided mode EMIC waves in general (Horne & Thorne, 1993).

Yuan et al. (2019) reported a He^+ band wave event associated with density variation, wave mode analyze suggesting that the waves belong to the guided mode. EMIC waves with quasi-constant frequency crossing a range of L -shell have been reported previously (e.g., Paulson et al., 2014, 2017; Tetrack et al., 2017; G. Wang et al., 2019, and others). One explanation for the events in G. Wang et al. (2019) is that the waves emitted from the sources may pass through the crossover frequency and bi-ion frequency, turning from the guided L-mode waves to the unguided R-mode waves (Hu et al., 2010; G. Wang et al., 2019). Such a process can also explain the origin of the R-mode waves observed on the ground (Feygin et al., 2007).

Up to now, there is a lack of observation that confirm the existence of the unguided L-mode EMIC waves (or the Class-II waves, as shown in Figure S1) according to the polarization characteristics. However, the hot H^+ with hundreds of keV can inject into the ring current during storms (Zhao et al., 2015), theoretically providing the energy source for the generation of unguided mode waves. Moreover, the smaller group velocities of unguided mode waves may lead to the larger convective growth rates, which can favor the wave generation (Horne & Thorne, 1994). The motivation of the present study is based on the following questions: Can we find the distinguishable unguided mode EMIC waves that are locally generated below f_{cH^+} ? If so, what's the difference in the generation mechanism between the guided and unguided mode waves? Here we identify the existence of the intense unguided mode EMIC waves in the earth's radiation belt by presenting Van Allen Probe (Mauk et al., 2013) observations. We will propose that the generation of these waves is associated with a new type of wave trapping mechanism, which is controlled by the spatial variation of ion abundance ratios.

2. Data and Methods

2.1. Extraction of Wave Properties

The magnetic field data from MAG, and the electric field data from EFW are used to analyze the wave properties. The 64 Hz magnetic field data are processed through a 1024-point fast Fourier transform (FFT, without detrending) to obtain the magnetic spectral matrix. Singular value decomposition (SVD) analysis (Santolík et al., 2003) is performed on the magnetic spectral matrix to estimate the wave normal angle, azimuthal angle, and wave polarization (Santolík et al., 2003). The 32 Hz two-dimensional electric field data from EFW are used to estimate the vector electric field, and the spin axis-aligned component is estimated with the assumption that $\mathbf{E} \cdot \mathbf{B} = 0$. The error may be large when B_z is small, which is not the case for the parallel waves measured by Van Allen Probes as their spin axes are approximately in the equatorial plane (Mauk et al., 2013). A 512-point FFT is carried out for both the electric field and the magnetic field

(resampled to 32 Hz) to obtain the cross-power spectra, and thus, we obtain the Poynting vector (Santolík et al., 2010). The technical details are the same as G. Wang et al. (2019).

2.2. Plasma Conditions for Calculating Wave Growth Rate

The linear growth rate described in the appendix can be estimated based on observations. The derivatives of the phase space density ($F = j/p^2$) with respect to the energy E and pitch angle α for each ion species can be obtained based on observation of the Helium, Oxygen, Proton, and Electron (HOPE) mass spectrometer (Funsten et al., 2013) and the Radiation Belt Storm Probes Ion Composition Experiment (RBSPICE) instrument (Mitchell et al., 2013). As the major ions H^+ dominate the wave growth, here the phase space density F is estimated approximately from the H^+ flux collected by HOPE and RBSPICE. HOPE measures the H^+ flux (j_{H^+}) with the energy from several eV to ~ 50 keV, while the RBSPICE measures j_{H^+} from ~ 50 keV to ~ 600 keV. These two energy ranges cover the main structures of the ring current H^+ and are sufficient to evaluate the linear instability. The HOPE flux is multiplied by a factor of three so that the mismatch between the low-energy part of RBSPICE and the high-energy part of HOPE can be eliminated (Kistler et al., 2016; Min et al., 2017). The distribution of $F(E, \alpha)$ is fitted along pitch angle α for each fixed energy channel, and the required derivatives are then approximated with the help of B-spline interpolation. The details regarding this technique follow (Liu et al., 2018). The zero-order $D^{(0)}$ and first-order $D^{(1)}$ of the dispersion matrix are also depend on the background magnetic field, the plasma number density n_e and the ion abundance ratios $\eta_s = n_s/n_e$ (where s denotes the particle species) besides phase space density F (Kennel, 1966). The magnetic field is measured by the triaxial fluxgate magnetometer (MAG), the local plasma density is measured by the High Frequency Receiver (HFR) (Kurth et al., 2015) of the Electric and Magnetic Field Instrument and Integrated Science (EMFISIS) suite (Kletzing et al., 2013). The ion abundance ratios are determined via the plasma diagnostics as described in the appendix.

3. Observations

3.1. Overview of the Event

As shown in Figure 1a, the event was observed by Probe A on December 15, 2015, during the recovery phase of a magnetic storm, after at least three successive prominent substorms where $AE > 500$ nT. In Figure 1b–c, the hot H^+ fluxes enhance in four distinct energy ranges: below 10 keV, 10–30 keV, 30–100 keV and 100–600 keV. The peak energy of the hot H^+ for each energy range decreases with L -shell, indicating the energy-dispersive substorm injected ions (Zhao et al., 2015). From Figure 1d, the satellite passed through the plasmapause at $L \sim 2.87$, and the background electron number density n_e measured by HFR dropped from $\sim 100 \text{ cm}^{-3}$ at just outside the plasmapause to $\sim 20 \text{ cm}^{-3}$ at $L \sim 3.7$. The conspicuous H^+ band waves appear from $L \sim 3.1$ to $L \sim 3.7$, as exhibited in Figure 1e. These waves with quasi-constant frequencies appear to be intense just outside the plasmapause and decay gradually with the increasing L -shell.

3.2. Wave Analyses and Ion Abundance Ratios

The wave properties are presented in Figure 2. In general, the time series of the wave spectra can be divided into three distinct regions based on the observational characteristics, as marked by the blue boxes. The Region A waves appear at MLAT $\sim -1.5^\circ$, have the strongest magnetic spectral density PSD_B , associated with the quasi-parallel wave normal angle ψ and small compressional ratio $PSD_{B\parallel}/PSD_B$, indicating that they were propagating roughly along the ambient magnetic field. Furthermore, the general direction (shown by the diamonds, which are the spectrum-weighted averages) of the Poynting fluxes appears to be northward for the inner waves, and be southward for the outer waves (Figure 2f), and almost all these intense waves possess a slight inward orientation (Figure 2e). The results of the ellipticity ϵ_B show predominately left-hand polarization, indicating that the waves belong to the L-mode. In Region B, the waves show a decrease in PSD_B of approximately one order. Noticeably, the ϵ_B spectra show a sharp boundary which separates the left-hand and right-hand polarization, indicating the pass-through of the He^+ crossover frequency f_{crHe^+} . Independent of the polarization, the waves with different values of the wave normal angle or compressional ratio are highly mixed. The outermost waves are presented in Region C, with a wave power 2 orders

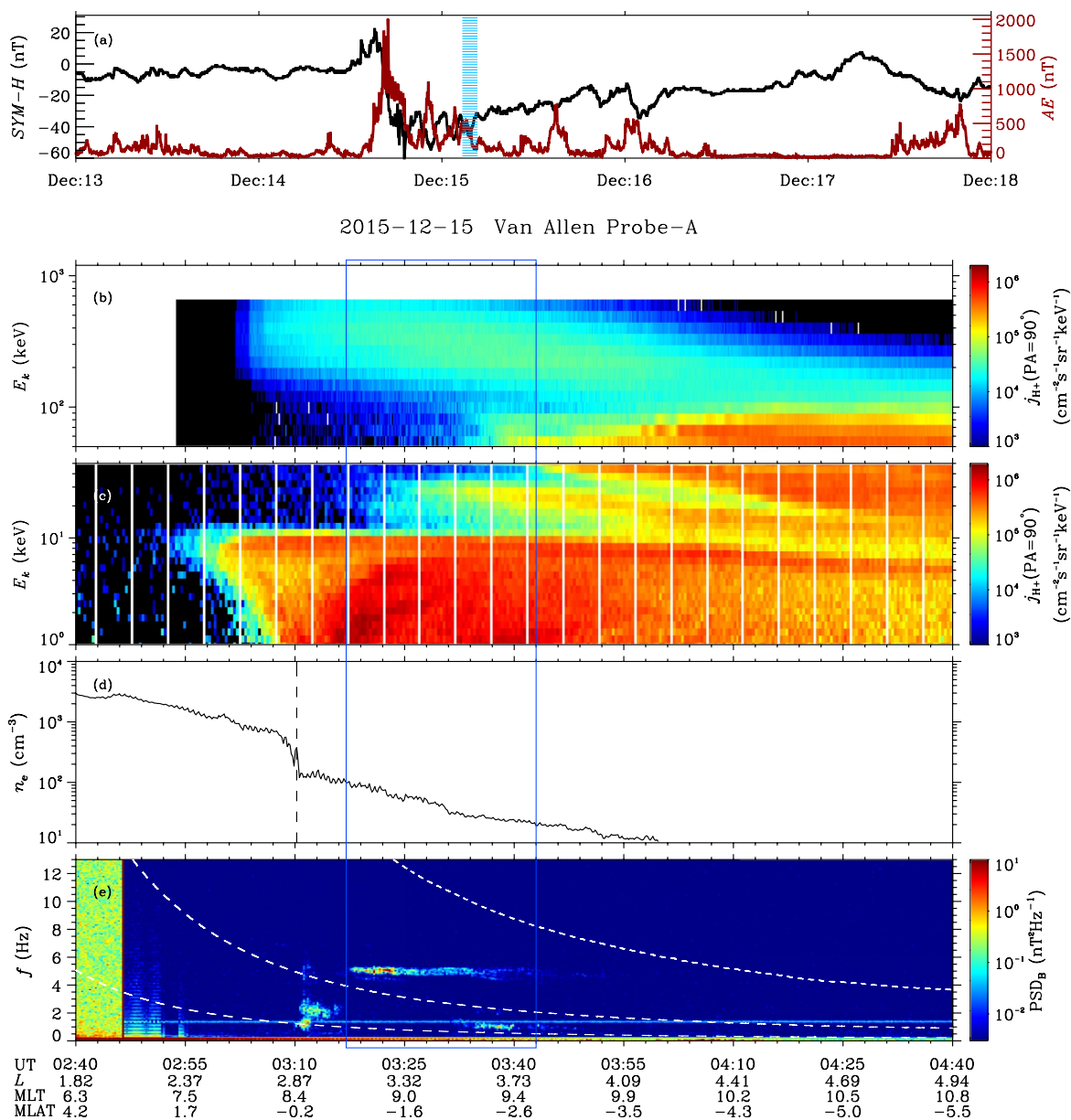


Figure 1. Overview of the wave event recorded by Van Allen Probe A on December 15, 2015: (a) SYM-H index and AE index (shaded region marks the period of the wave event). (b) Background electron number density n_e (dashed lines for the location of the plasmapause). (c and d) Energy-dependent H^+ differential fluxes j_{H^+} at a 90° pitch angle measured by Radiation Belt Storm Probes Ion Composition Experiment and ECT HOPE. (e) Magnetic power spectral density PSD_B . The white dashed curves trace the local gyrofrequencies of hydrogen, helium, and oxygen. The blue box marks the period of the wave event.

of magnitude smaller than that of the waves in Region A. The wave vectors are almost perpendicular to the ambient field, the compressional ratios are relatively large, and the polarizations are predominantly right-handed, indicating these are the oblique R-mode waves.

With increasing L -shell value, the relative frequency f/f_{ch+} increases for the observed H^+ band waves with a quasi-constant frequency, and the polarization mode thus changes from L-mode to R-mode. Such a phenomenon indicates that the waves belong to the unguided mode (Rauch & Roux, 1982), as illustrated in Figure 2j. Here, we perform the plasma diagnostics to verify the wave mode and estimate the ion abundance ratios η_s . As shown by Figures 2c and 2a series of f_{crHe+} can be obtained for a given group of η_s according to Equation A2. Assuming that the boundary where the polarization reversal takes place (the blue solid curve) represents the trace of f_{crHe+} , one can obtain $\eta_{H^+} \sim 83\%$ and $\eta_{He^+} \sim 17\%$ by solving Equation A2 numerically.

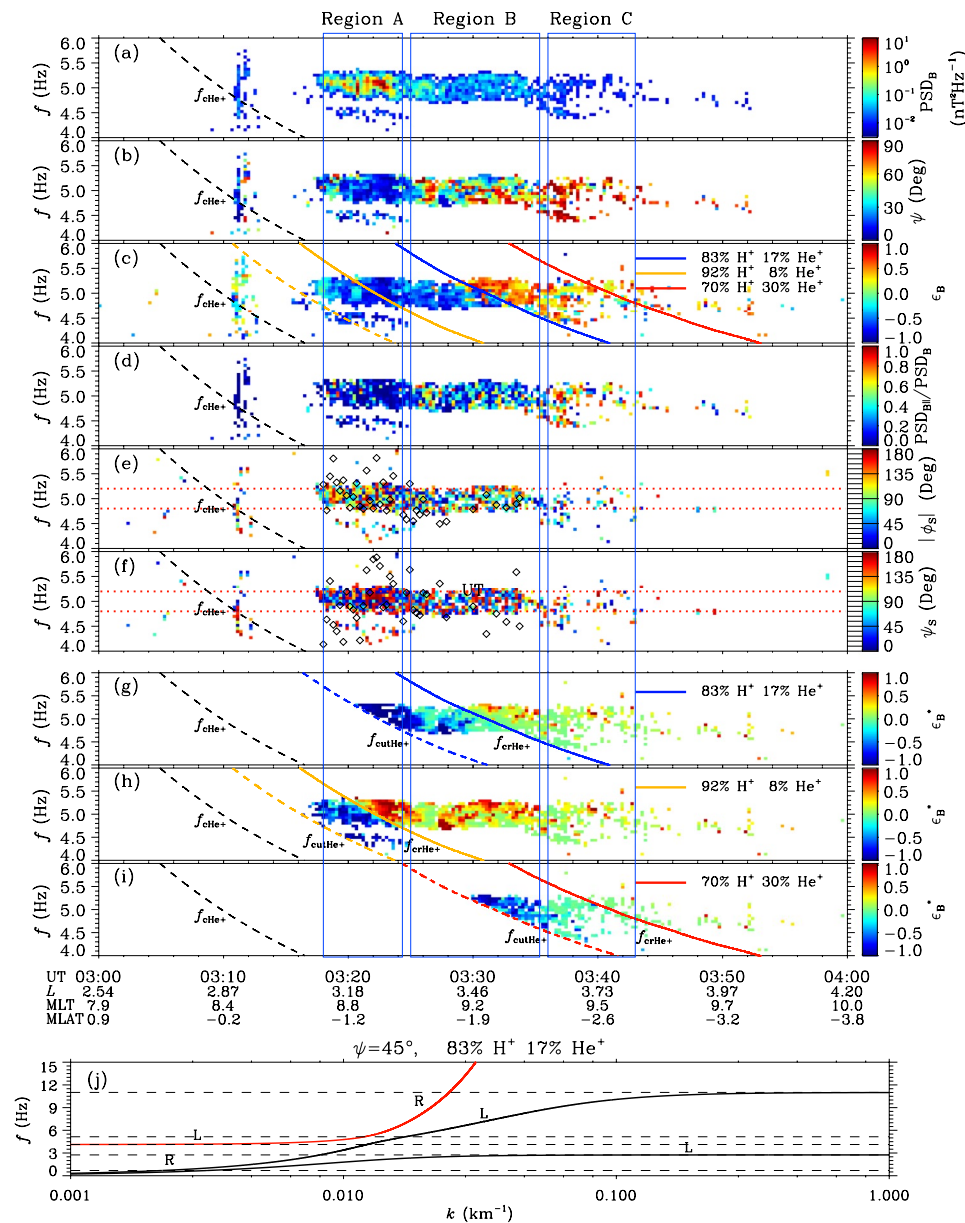


Figure 2. Analyses of wave properties and wave mode. (a) Magnetic power spectral density PSD_B . The blue boxes roughly separate the three distinct regions with different observational characteristics. (b) Wave normal angle ψ (unifying the two field-aligned orientations). (c) Wave ellipticity ϵ_B . The negative value represents the left-hand polarization. (d) Wave magnetic compression ratio PSD_{B_i}/PSD_B . (e) The azimuthal angle of the Poynting flux ϕ_s (0° represents away from the Earth). (f) The angle of the Poynting flux with respect to the ambient magnetic field ψ_s . Black diamonds in (e and f) are the spectrum-weighted averaged angles within the frequency range of $4.8 - 5.2$ Hz (red dotted lines), and they share the same axis with the corresponding color bars. (g-i) The theoretically calculated distribution of the ellipticity ϵ_B^* for the given ion abundance ratios. The colored solid and dashed lines trace the local crossover frequencies f_{crHe+} and cutoff frequencies f_{cutHe+} . (j) Dispersion relations under the observed plasma conditions. The red curve represents the observed wave mode. The letter “L” and “R” denote the left-hand and right-hand polarizations, respectively.

Substituting the obtained η_s and the observed ψ (Figure 2b) into Equations A7 and A8, one can obtain the theoretically estimated ellipticity ϵ_B^* . As shown in Figure 2g, the polarization reversal boundary does exist for the estimated ϵ_B^* spectra and generally matches the observed boundary. However, the waves observed before 03:20 UT cannot be seen in the ϵ_B^* spectra, suggesting that the cutoff frequencies are overestimated

in these inner L -shell under the assumption of $\eta_{H^+} \sim 83\%$ and $\eta_{He^+} \sim 17\%$. Considering that the background plasma density decreases prominently with L in the range where the wave exists (from $\sim 100 \text{ cm}^{-3}$ at $L \sim 3.1$ to $\sim 50 \text{ cm}^{-3}$ at $L \sim 3.3$ according to Figure 1d), one can assume that η_s may also vary with L , leading to the rapid change of cutoff frequencies. Assuming that the cutoff frequencies lie just below the lowest frequencies of the observed intense waves (the yellow dashed curve in Figures 2c and 2h), a new group of η_s can be obtained by numerically solving Equation A9: 92% H^+ and 8% He^+ . As shown in Figure 2h, the ϵ_B^* spectra contain the lower-frequency waves observed before 03:20 UT under this group of ion abundance ratios. In addition, a group of η_s is provided in Figure 2i for comparison, where both the cutoff frequency and the polarization distribution deviate from the observations significantly. These results confirm that the polarization reversal boundary is the time series of f_{crHe^+} in the unguided mode, and suggest that the H^+ abundance decreases from at least 92% at $L \sim 3.2$ to approximately 83% at $L \sim 3.5$ where the polarization reversal takes place.

The field-aligned and anti-field-aligned Poynting fluxes and the strong wave power, strongly indicate that there are overlaps between Region A and the wave source region (Allen et al., 2013; Loto'Aniu et al., 2005; Vines et al., 2019). The waves in Region B and Region C can be the leaked waves from the source, or the locally excited waves with oblique wave normal angles. We will explore the origin of these waves in the following section.

4. Wave Growth Mechanism

4.1. Linear Growth Analyses

To reveal the generation mechanism of the observed unguided mode waves, we first present the results of the linear convective growth rate in Figure 3, following the method in Liu et al. (2018). Figures 3b and 3c show the convective growth rate distributions under the fixed η_s : $\eta_{H^+} = 92\%$ and $\eta_{He^+} = 8\%$. Positive growth rates appear below the local f_{crHe^+} , covering the ranges of the observed intense L-mode waves in the inner L -shell (Figure 3a). No wave growth can be obtained above f_{crHe^+} , due to the much higher resonant energy between H^+ and R-mode (Figure 3d). This result eliminates the possibility that the observed oblique R-mode waves in the outer L -shell are excited locally. From Figure 3e, as the minimum resonant energy is approximately 100 keV for the fundamental resonance of the parallel left-hand waves, the resonant surface avoids the hot H^+ rings with lower energies, but crosses the ring with the energy range of $\sim 200 - 450$ keV. The parameters crucial for the growth rate are presented in Figures 3f–3h. The maximum value of $G_{IH^+}^*$ appears within $E_k \sim 150 \text{ keV} - 200 \text{ keV}$, indicating the favorable energy range for the wave growth. However, the highest magnitude of the convective growth rate K_{H^+} is $\sim 10^{-7} \text{ m}^{-1}$ for the parallel waves (Figure 3b), therefore, the path-integrated wave gain should be a factor of at least $\sim 10^3$ (7 e-foldings), to satisfy the growth of the observed intense waves from the background noise level. This corresponds to an integrated traveling distance in the source adding up to $\sim 11 R_E$.

4.2. Potential Wave Trapping

The waves within the inner L -shell are intense and predominated by field-aligned wave vectors and Poynting fluxes but become weaker and more oblique outside. Moreover, the waves observed in all these regions have almost a constant frequency range. This evidence strongly implies that the waves are generated inside and propagated outward. The growth rate results further suggest this assumption by eliminating the possibility of oblique excitation for the outer right-hand waves. However, the most challenging problem is that the convective growth rate is too small for the observed strong waves generated in any potential source region with a limited spatial range. According to the previous analysis, an integrated traveling distance of $\sim 11 R_E$ in the source region is needed for the full growth of the parallel waves. It is reasonable to associate the convective growth process with some kind of wave trapping mechanism. As the hot ions are circling around the earth in the narrow range of the L -shell, the azimuthal propagation of the waves may provide the required integrated distance in one-half of the drift circle. However, this scenario contradicts the observed parallel component of the Poynting fluxes. Considering that the intense quasi-parallel waves are just above the local cutoff frequency f_{cutHe^+} , where the unguided mode waves should be reflected. To investigate the

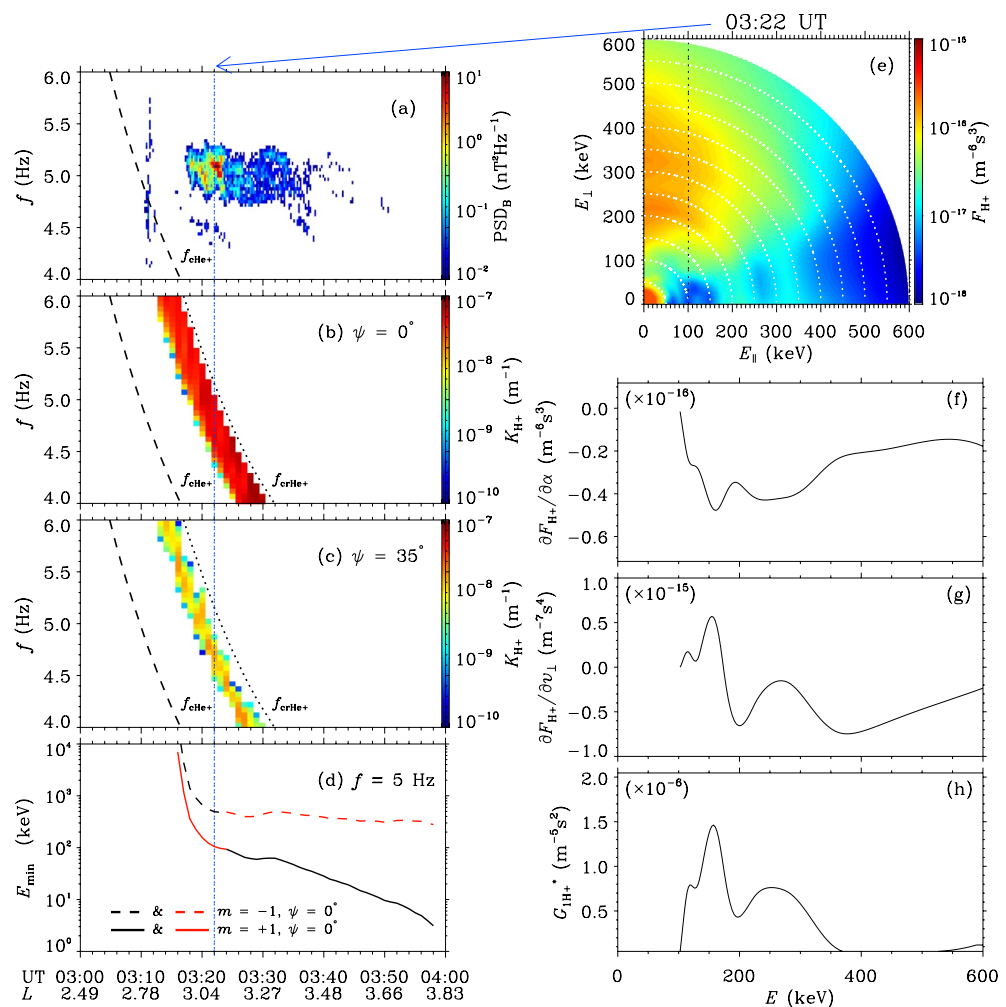


Figure 3. Wave growth analyses. (a) The observed magnetic power spectral density PSD_B . (b and c) Wave convective growth rates K_{H+} contributed by H^+ at different wave normal angles. The dotted curves trace the He^+ crossover frequencies while the dashed curves trace the He^+ gyrofrequencies. (d) Minimum H^+ resonant energy E_{\min} at a wave frequency of $f = 5$ Hz for different resonant orders. The red curves mark the resonance for the current unguided mode. (e) Distribution of the observed H^+ phase space density F_{H+} in the $E_{\perp} - E_{\parallel}$ space at the time point 03:22 UT. The dotted line represents the resonant surface for the fundamental resonance at the wave normal angle $\psi = 0^\circ$. (f–h) Energy dependence of $\partial F_{H+}/\partial \alpha$, $\partial F_{H+}/\partial v_{\perp}$ and G_{H+}^* along the resonant surface as shown in (e). Here α is the pitch angle, v_{\perp} is the perpendicular velocity of H^+ , and G_{H+}^* is the integrating factor in the growth rate expression.

possibility of wave trapping, the distributions of refractive indexes RI are calculated in the simplified background plasma environment. The magnetic fields are estimated using the T89 model, and the values along each field line are calibrated by multiplying the factor $B_{\text{obs}}/B_{\text{model}}$ (ratio of the observed and model estimated value at the intersection point between satellite orbit and field line). The density distribution is calculated by $\rho(MLAT) = \rho_{eq}/\cos(MLAT)$ with the help of the observations. As demonstrated in Figure 4a–b, in a plasma environment with constant η_s , the reflection interface where the refractive indexes RI decrease to zero is approximately perpendicular to the equatorial plane, because the value of $f_{\text{cutHe}^+}/f_{\text{cH}^+}$ remains the same while the value of f_{cutHe^+} decreases with radial distance but increases with latitude due to the variation of the magnetic field. As shown by Kim and Johnson (2016), the unguided waves will be reflected at f_{cutHe^+} and propagate to the larger L -shell under this condition. In the present case, the relative frequency $f_{\text{cutHe}^+}/f_{\text{cH}^+}$ should increase with η_{H^+} (or decrease of η_{H^+} , as shown in Figure 4c) at a higher L -shell, thus offsetting the effect of the magnetic field. The strong reflection interface formed by the locations of f_{cutHe^+} (where $RI = 0$) is therefore approximately parallel to the equatorial plane, as shown in Figure 4d. The conjugate

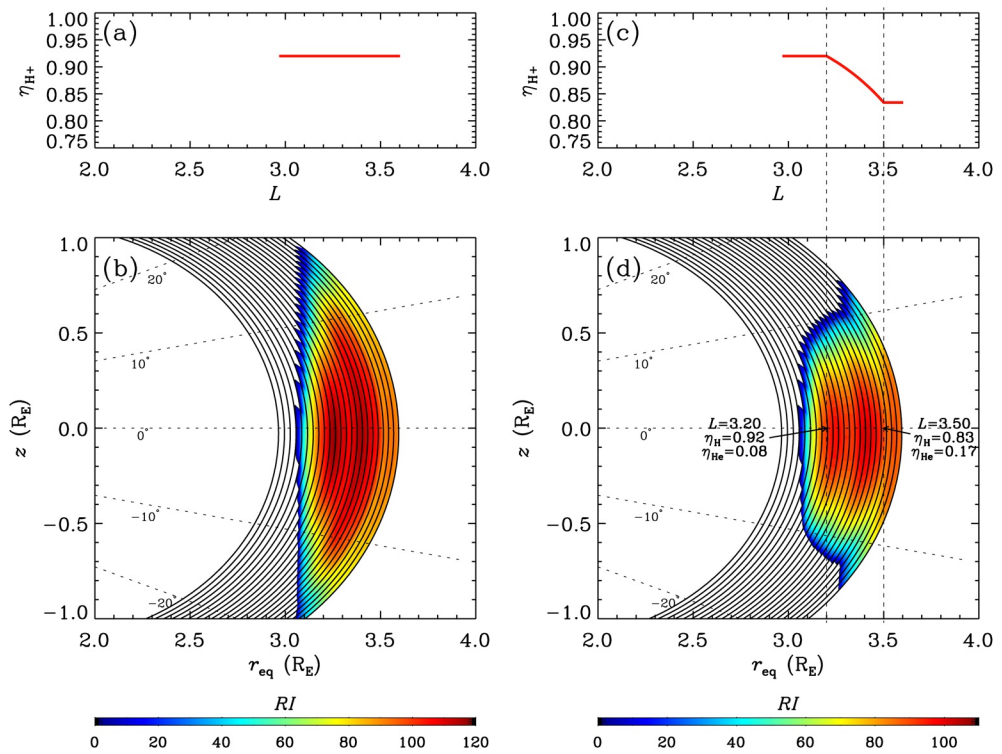


Figure 4. The distribution of the refractive index RI in a plasma environment with the ion abundance ratio η_{H^+} : (a and b) distributed uniformly and (c and d) varied with the L -shell. The coordinate system is established in the Earth's dipole field: the horizontal axis r_{eq} represents the radial distance to the dipole axis in the equatorial plane, while the z axis is along the dipole axis. Solid black curves trace the background magnetic field estimated with the help of the T89 model.

reflection interfaces in both sides of the equatorial plane may produce a trapping zone, within which some of the unguided mode waves will be trapped and experience the significant amplification to the observed intensity. In addition, as shown in Figure 2b, the plasma number density experiences a sharp change at approximately $L = 3.48$, which may result in a dramatic variation in η_s with L , and thus form a quasi-parallel or even negatively inclined reflection interface at the radial distance $\sim 3.2 - 3.3 R_E$. This is consistent with the strongest waves observed at $L \sim 3.2 - 3.3$ near the equator. Moreover, both the L-mode waves and the R-mode waves in Region B possess almost the same magnitude of wave power (Figure 2), suggesting that they are the leaked waves from the inner trapping region (polarization reversal process does not influence the wave power). Following such a scenario, one can predict that the waves observed away from the trapping region should propagate in the direction pointing from the trapping region to the observed position, which can explain the quasi-perpendicular waves observed in Region C.

5. Discussion

5.1. Reliability of Linear Theory for Explaining Observations

The estimated values of linear growth rates are too small to explain the observed wave intensity without the wave trapping. Blum et al. (2009) developed the two-parameter proxy of EMIC growth based on linear theory (Gary, 1993), and found an association between EMIC growth and relativistic electron loss during storms. The linear growth proxy can well predict the statistical wave enhancement regions (Allen et al., 2016) as well as the specific wave events (J.-C. Zhang et al., 2014). However, Saikin et al. (2018) found that the calculated wave amplitudes are too low compared to the observation. As far as our information goes, the following reasons may be responsible for the mismatches between calculations and observations: nonlinear effects (Omura et al., 2010); inaccurate plasma conditions, for example, the bi-Maxwellian distribution assumption, the assumed ion abundance ratios, the model predicted electron density, and the neglecting of the hot ions of a few hundred keV (J. H. Lee et al., 2021; Saikin et al., 2018); the ambiguity of wave propagation and

convective growth (Thorne & Horne, 2007; Khazanov et al., 2007); the marginally stable assumption (Gary & Lee, 1994; Yue et al., 2019; Yu & Yuan, 2019).

Nonlinear effects tend to suppress wave amplitude for the intense waves (Min et al., 2015; Omura et al., 2008), thus are not likely to lead to the underestimation of wave growth in the linear approach. In the present calculations, the ion distributions are based on observations, the assumed ion abundance ratios are derived from observed crossover frequency and cutoff frequency, and the hot ions of a few hundred keV are considered, therefore, all the plasma condition parameters in the linear growth rate are more realistic.

For the guided mode, the wave behaviors near bi-ion frequency are complex, and the proportions of energies that experience absorption, transmission, or reflection are highly dependent on the ion abundance ratios (Horne & Throne, 1997; Hu et al., 2010; Khazanov et al., 2006; Thorne & Horne, 1993). Therefore, the ambiguity of ion abundance ratios may lead to the improper estimation of the integrated wave gain. In addition, the present study indicates that the spatial variation of ion abundance ratios may also influence the propagation of guided waves near the bi-ion frequency, which may be a candidate, besides the oblique excitation by heavy ions (Denton et al., 1992; Gamayunov et al., 2018; Hu & Denton, 2009; Hu et al., 2010), to explain the origin of previously reported oblique linear or right-hand EMIC waves in the inner plasmasphere (Allen et al., 2015; Grison et al., 2016; Min et al., 2012; Saikin et al., 2015; G. Wang et al., 2019) or away from general peak occurrence regions (Wang, Huang, et al., 2017). Unlike the guided mode, the convective growth for the unguided mode is relatively simple, because the refractive index is approximately independent of the wave normal angle, which allows us to predict the wave behavior solely based on the global plasma conditions. Furthermore, as the wave vectors are approximately parallel to the magnetic field for the rays with parallel group velocity, Landau damping should not be prominent (Thorne & Horne, 1992) (Landau damping rate should be zero for parallel \mathbf{k} [Kennel, 1966]); and as the wavenumbers are small near cutoff frequency, cyclotron damping by heavy ions should also be insignificant (Thorne & Horne, 1993).

Yue et al. (2019) demonstrated an upper limit of growth rate for EMIC waves based on the observed ion distributions, indicating the importance of local growth, that is, the disturbance intensity of the wave source may be dependent on the time integration. This scenario of the local growth of wave source makes the trapping and convective growth “unnecessary,” for the explanation of the observed wave intensity. The problem that either the local growth or the convective growth determines the observed wave amplitude in the source region cannot be exactly solved based on the present observations, however, we can still do some exploration. According to X. Yu and Yuan (Yu & Yuan, 2019), it typically needs a period of tens of minutes for a wave source to reach the saturation state without injection of free energy. Considering the western drift of hot ions with a speed of several km/s (for 10 keV), for the typical EMIC event with a scale size of $\sim 0.5L$ (Blum et al., 2017), the time scale of the refresh of anisotropy should be comparable with that of the saturation. In the present event recorded by Probe A on December 15, 2015, considering that the drift speed of 200 keV protons at $L = 3.2$ is approximately 30 km/s, and the calculated growth rates are relatively small, the observed hot proton distributions are more likely to be in the “fresh” state. From Figure 3, the values of the calculated convective growth rates are in the same order of magnitude in the selected time-frequency region, does not match exactly the variation of the observed wave intensity, further indicating that the anisotropy is not significantly relaxed within the source region (otherwise the calculated growth rate should be relatively smaller in the region of intense waves) (Gary & Lee, 1994; Yu & Yuan, 2019). Furthermore, the growth rates of the guided mode waves (please see Figure S3) are in the same order of magnitude as that of the unguided mode waves (Figure 3). As the guided mode waves should experience imperfect reflection and wave vector obliquity, which may substantially reduce the repeated convective amplification (Horne & Throne, 1993; Hu et al., 2010; Loto'Aniu et al., 2005), if the actual generation process of the observed unguided mode waves is also not significantly influenced by the reflection and convective amplification, the guided mode waves are supposed to be observed with the same intensity of the unguided mode waves. Considering that only the unguided mode waves are observed, and that the intense waves are just located within the predicted trapping region, the process of trapping and convective amplification may be important to facilitate the wave generation.

5.2. Spatial Inhomogeneity of Ion Abundance Ratios

The spatial distributions of the ion abundance ratios η_s in the inner magnetosphere have considerable uncertainty. The statistics using Dynamics Explorer-1 (DE-1) showed that the $\eta_{\text{He}^+} / \eta_{\text{H}^+}$ ratio decreases with L below $L \sim 2$ but increases with L over $L \sim 2 - 5$ (Goldstein et al., 2019). The magnetoseismology study by Takahashi et al. (Takahashi et al., 2006) revealed that the average ion mass during the quiet period is $\sim 2.0 - 3.0$ outside the plasmasphere (identified by n_e larger than 100 cm^{-3}) but is lower than 2.0 inside the plasmasphere. Therefore, there is a general trend that the proton abundance increases from outside the plasmasphere to just inside the plasmasphere. In the event recorded by Probe A on December 15, 2015, the value of η_{H^+} decreases from 92% at just outside the plasmapause (n_e is approximately 100 cm^{-3}) to 83% at higher L (n_e is approximately 30 cm^{-3}), as shown in Figure 2. The value of η_{H^+} increases with n_e in this result, consistent with the trends from previous studies. Moreover, the model-estimated values of $\eta_{\text{He}^+} / \eta_{\text{H}^+}$ according to Huba and Krall (2013) are approximately 5% – 10% in the outer plasmasphere, corresponding to the present estimated values near the plasmapause. Therefore, the present results are consistent with the previous studies that the substantial spatial variation of ion abundance ratios may exist in the vicinity of the plasmapause. In addition, the O^+ abundance ratio η_{O^+} has been neglected in the main analyses (based on Appendix A). In a more reality case of 5% η_{O^+} (Bashir & Ilie, 2018; Miyoshi et al., 2019), as demonstrated in Figure S4, the trend of decreases of η_{H^+} (from 89% to 82%), the peak values of linear growth rate, and the predicted trapping region have no substantial differences with the corresponding results neglecting O^+ .

5.3. How Prevalent are the Unguided Mode EMIC Waves?

During the period from September 2013 to May 2018, another obvious event of unguided mode waves with a distinguishable crossover frequency was recorded by Probe A on November 30, 2015, when the satellite was outside the plasmasphere (please see Figure S5). A similar trend of the spatial variation of ion abundance ratios can be obtained based on plasma diagnostics (Figure S6), indicating the potential existence of wave trapping. The intense L-mode waves are observed along with the enhancement of hot H^+ with the energies of hundreds of keV, while the positive convective growth rates are obtained (Figure S7). The magnitude of largest growth rates is approximately several times of 10^{-7} m^{-1} , which is inadequate for the waves to be amplified to the observed magnitude (more than 7 e-foldings) in an integrated distance less than $1 R_E$. As the waves are observed near the equatorial plane, one can thus predict that the wave trapping mechanism may have played an important role in the amplification of the observed waves.

The event in the previous section was recorded by Probe A. In fact, Probe B also recorded a wave event in the same area ~ 2 h earlier. As shown in Figure 5, the intense H^+ band waves were observed at $L \sim 3.16$, $MLT \sim 8.5$ and $MLAT \sim -1.2$, which were within exactly the same area of Probe-A-event. Comparing Figures 1 and 5, the background plasma conditions are also similar for these two probes during their respective passes, that is, waves were observed just outside the plasmasphere, with the enhancement of hot protons of hundreds of keV. In the event of Probe B, a weak “tail” toward the higher L -shell and larger value of f/f_{cH^+} can also be observed. This “tail” can be explained by the outward propagation of the unguided mode waves. In this event, however, no obvious boundary of R-mode and L-mode can be distinguished, as shown in Figure 6. Therefore, we cannot determine the mode of these waves based on the observations. It is possible that the configuration of the potential trapping region restricts the intense waves below crossover frequencies. However, as the plasma conditions are the same as that of Probe-A-event, and the weak ‘tail’ may indicate the propagation toward higher L -shell, it is reasonable to suppose that these waves are the unguided mode waves, being trapped and amplified with the same mechanism as the waves in Probe-A-event (Figures S8 and S9 show the growth rates). If so, as these waves do not have an obvious right-hand polarization, they cannot be distinguished from the guided mode waves, maybe they are common in the radiation belt and are intermixed with the guided mode waves in the previous studies. The exact measurements of ion abundance ratios are needed for identification of these different modes, in the cases with the crossover frequencies unidentifiable.

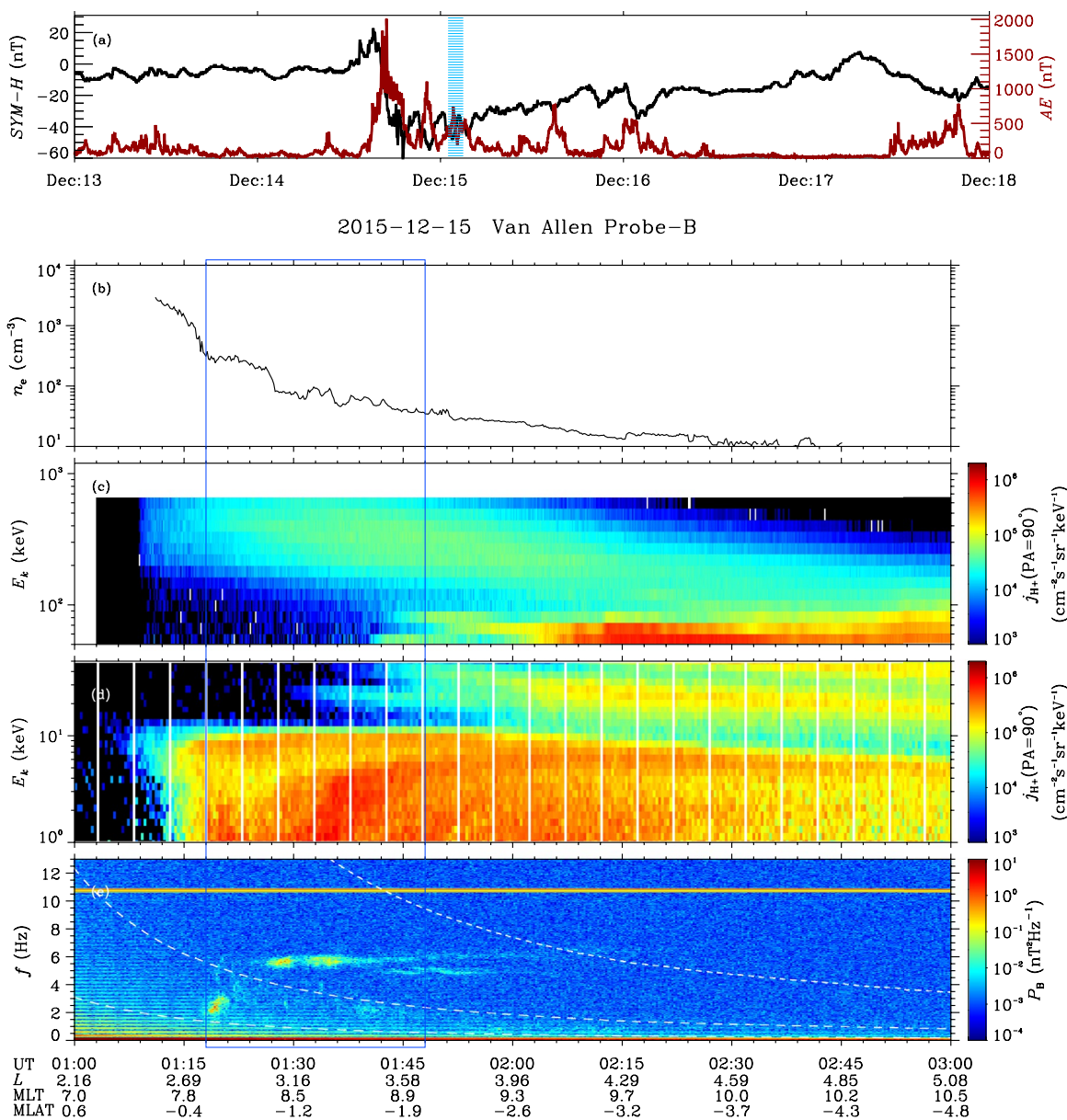


Figure 5. Overview of the unguided mode wave event recorded by Probe B on 15 December 2015: (a) SYM-H index and AE index (shaded region marks the period of the wave event); (b) background electron number density n_e (dashed lines for the location of the plasmapause); (c and d) energy-dependent H^+ differential fluxes j_{H^+} at a 90° pitch angle; and (e) magnetic power spectral density P_B (white dashed curves trace the local gyrofrequencies of hydrogen, helium, and oxygen from top to bottom).

6. Summary

From previous studies, EMIC waves can scatter relativistic electrons (e.g., Blum et al., 2015; Cao et al., 2017; Miyoshi et al., 2008; Ni et al., 2015; Omura & Zhao, 2013; Rodger et al., 2015; Su et al., 2017; Usanova et al., 2014; Z. Wang et al., 2014; Wang, Su, et al., 2017; X. J. Zhang et al., 2016; Zhu et al., 2020, and others), lead to the decay of ring current ions (Daglis et al., 1999; Fuselier et al., 2004; Su et al., 2014), or heat the cold electrons (Thorne et al., 2006; Yuan et al., 2014). The present study clearly demonstrates the existence of unguided mode EMIC waves in the radiation belt, and propose a trapping and amplification mechanism for explaining their origin. The results are summarized here:

1. H_+ band waves with quasi-constant frequencies were observed near the equatorial plane. Intense waves with quasi-parallel wave normal angles and left-hand polarizations appeared just outside the pre-noon

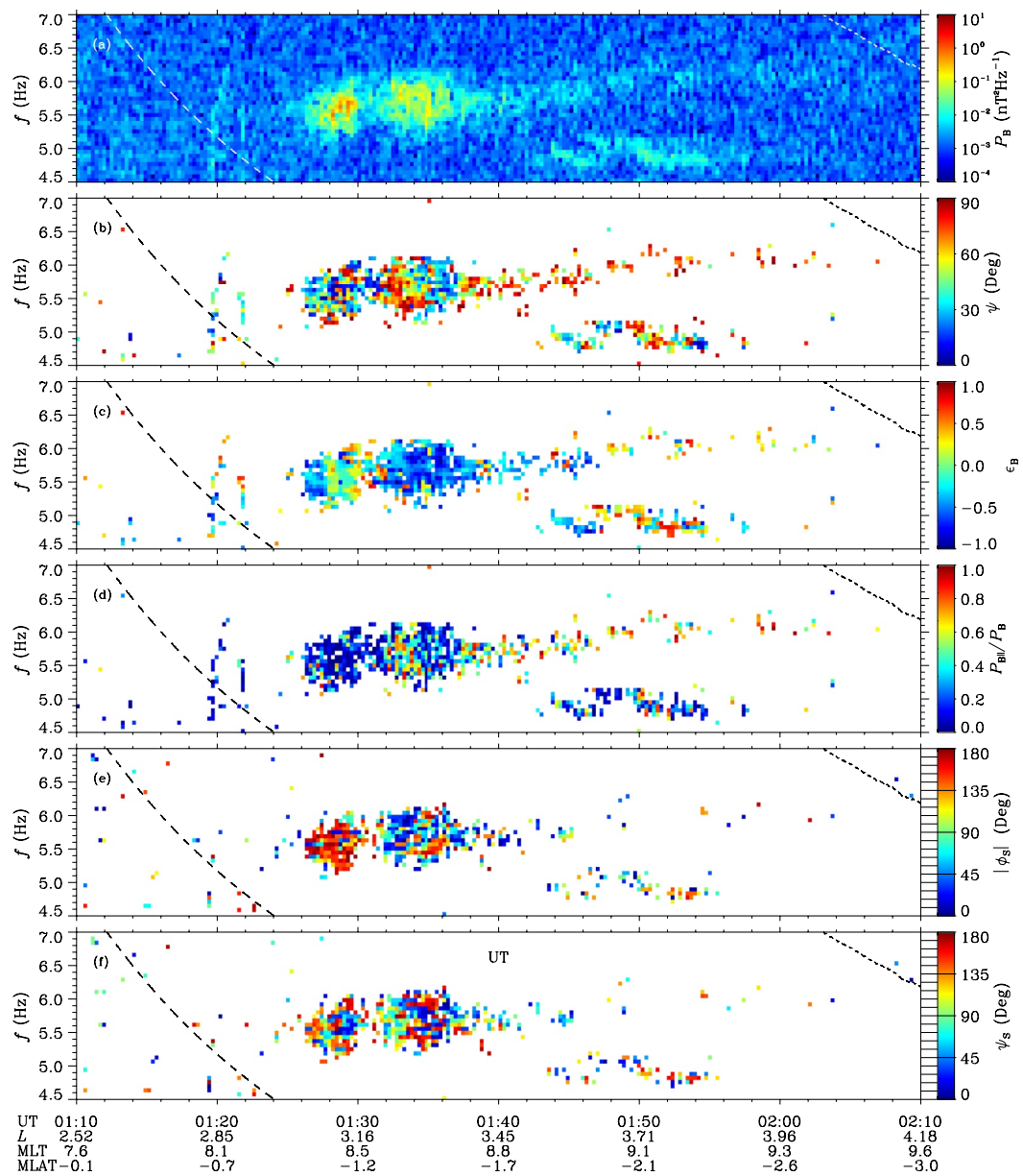


Figure 6. Wave properties of the event recorded by Probe B on December 15, 2015: (a) magnetic power spectral density P_B , (b) wave normal angle ψ (unifying the two field-aligned orientations), (c) ellipticity ϵ_B , (d) magnetic compression ratio $P_{B\parallel}/P_B$, (e) azimuthal angle of the Poynting flux ϕ_s (0° represents away from the Earth), and (f) angle of the Poynting flux with respect to the ambient magnetic field ψ_s .

plasmapause. With increases in the L -shell and the relative wave frequency $f/f_{\text{ch+}}$, the wave vectors became oblique, and an obvious boundary where the wave polarization reversed from left-handed to right-handed was observed. Plasma diagnostics verified that the waves belonged to the unguided mode, and the proton abundance ratio may decrease with the L -shell.

2. Weak linear growth rates contributed by hot protons with a few hundred keV were obtained in the regions of intense parallel L-mode waves, where a source-integrated distance of approximately $11 R_E$ is needed for the convective growth of the L-mode waves to the observed wave power.
3. The reflection boundary formed by the spatial distribution of the local helium cutoff frequencies was investigated. Under the condition of a sharp decrease in the proton abundance ratio with increasing L -shell, the reflection boundary can be nearly parallel to the equatorial plane. As the unguided L-mode

waves should be reflected at the reflection boundary, this structure combined with hot protons of a few hundred keV may serve as an amplifier for the generation of the observed class-II waves.

These results may have potential importance for understanding the dynamics of the Earth's radiation belt.

Appendix A: Plasma Diagnostics

In the cold plasma, the following Stix parameters are helpful to investigate the dispersion relation (Stix, 1992):

$$L = 1 - \sum_s \frac{\omega_{ps}^2}{\omega(\omega - \Omega_s)}, R = 1 - \sum_s \frac{\omega_{ps}^2}{\omega(\omega + \Omega_s)}, P = 1 - \sum_s \left(\frac{\omega_{ps}}{\omega} \right)^2, \quad (A1)$$

Here, $\omega_{ps} = (n_s q_s^2 / m_s \epsilon_0)^{1/2}$ and $\Omega_s = q_s B / m_s$ are respectively the plasma frequency and the gyrofrequency of a particle species s .

The crossover frequency f_{cr} and the cutoff frequency f_{cut} can connect the observations to the dispersion relation. f_{cr} is the frequency where the L-mode and R-mode phase velocities are equal (Smith & Brice, 1964) and can be obtained by setting the Stix parameter L equal to R:

$$\sum_s \frac{\omega_{ps}^2}{\omega_{cr}(\omega_{cr} - \Omega_s)} = \sum_s \frac{\omega_{ps}^2}{\omega_{cr}(\omega_{cr} + \Omega_s)}. \quad (A2)$$

Considering the charge neutrality condition, the determination of full ion abundance ratios requires the values of at least two characteristic frequencies (except gyrofrequencies) to be known in H^+ , He^+ and O^+ plasma. However, if the O^+ abundance η_{O+} is much lower than the H^+ abundance η_{H+} and if the focused mode belongs to the H^+ band which has a much larger frequency than the oxygen gyrofrequency Ω_{O+} , then we have the following relations:

$$-\frac{\omega_{pH+}^2}{\omega(\omega - \Omega_{H+})} \gg \frac{\omega_{pO+}^2}{\omega(\omega - \Omega_{O+})}, \text{ when } \Omega_{He+} < \omega < \Omega_{H+} \quad (A3)$$

$$\frac{\omega_{pHe+}^2}{\omega(\omega - \Omega_{He+})} \gg \frac{\omega_{pO+}^2}{\omega(\omega - \Omega_{O+})}, \text{ when } \omega \rightarrow \Omega_{He+} \quad (A4)$$

$$\frac{\omega_{pH+}^2}{\omega(\omega + \Omega_{H+})} \gg \frac{\omega_{pO+}^2}{\omega(\omega + \Omega_{O+})}, \text{ when } \Omega_{He+} < \omega < \Omega_{H+} \quad (A5)$$

$$\frac{\omega_{pH+}^2}{\omega^2} \gg \frac{\omega_{pO+}^2}{\omega^2}, \text{ when } \Omega_{He+} < \omega < \Omega_{H+}. \quad (A6)$$

Therefore, if the three-ion (H^+ , He^+ and O^+) plasma are approximated as two-ion (H^+ and He^+) plasma, that is, the terms with oxygen plasma frequency ω_{pO+} are dropped in Equation A1, the Stix parameters will have only a negligible change (example in Figure S2). Under such an approximation, a group of ion abundance ratios (η_{H+} and η_{He+}) can be obtained by substituting the observed value of $\omega_{crHe+}/\Omega_{H+}$ into Equation A2. Consequently, the approximated dispersion relations for the modes in H^+ band can be found.

As the wave magnetic field vector is always perpendicular to the wave vector (i.e., $\mathbf{B} \cdot \mathbf{k} = 0$) for a plane electromagnetic wave, it is reasonable to define the polarization state in terms of the wave magnetic field, which is perpendicular to \mathbf{k} . The polarization state should include two aspects: rotation sense and polarization ellipse. As the sense of wavefield rotation about the ambient magnetic field \mathbf{B}_0 remains the same for a certain polarization mode, it is convenient to define the rotation sense in terms of \mathbf{B}_0 . As the wave magnetic field vector lies in the plane perpendicular to \mathbf{k} , it will convey more complete information by calculating the polarization ellipse in \mathbf{k} -centric frame. Based on these considerations, the polarization state can be represented

by the ellipticity ϵ_B . The magnitude of ϵ_B represents the polarization ellipse, while negative values for left-hand polarization and positive values for right-hand polarization (see Figure S1).

ϵ_B changes sign upon crossing f_{cr} . For the observed polarization reversal, a validation of whether it represents the crossover frequency f_{cr} can be performed by comparing the distribution of the observed ellipticity ϵ_B with the theoretically predicted ellipticity ϵ_B^* . Previous studies have expressed the ratio of the wave magnetic field in the coordinate system with the z -axis along \mathbf{B}_0 and the y -axis perpendicular to the $\mathbf{B}_0 - \mathbf{k}$ plane (Tao & Bortnik, 2010; Bortnik & Thorne, 2010):

$$\frac{B_x}{B_y} = -\frac{(R-L)(P-n^2 \sin^2 \psi)}{P(R+L-2n^2)}, \quad (\text{A7})$$

where ψ is the wave normal angle. The field amplitude can be transformed into the coordinate system with the z -axis along \mathbf{k} :

$$B'_x = \frac{B_x}{\cos \psi}, \quad B'_y = B_y, \quad (\text{A8})$$

the theoretically predicted ellipticity ϵ_B^* is then obtained considering that B'_x and B'_y are axes of the polarization ellipse.

In summary, the ion abundance ratios are estimated as follows: first, estimate the potential crossover frequency from the observed polarization of H^+ band waves; then, estimate the H^+ and He^+ abundance ratios by Equation A1; finally, compare the observed ellipticity ϵ_B with the calculated theoretical ellipticity ϵ_B^* for verification.

The cutoff frequency f_{cut} is the frequency where the phase velocity equals to zero (Smith & Brice, 1964), and can be obtained by setting the Stix parameter L equal to zero:

$$1 - \sum_s \frac{\omega_{ps}^2}{\omega_{\text{cut}}(\omega_{\text{cut}} - \Omega_s)} = 0. \quad (\text{A9})$$

Theoretically, the vanishing of waves below the lowest frequency of the observed wave power spectrum (denoted as f_{\min}) may be simply a result of a decrease of wave growth, which is due to the hot ion distribution and resonant conditions rather than the effect of the cutoff frequency. Therefore, the lower limit of the H^+ abundance ratio can be estimated by inserting the relation $f_{\min} \geq f_{\text{cut}}$ into Equation A9.

Appendix B: The Convective Growth Rate for Unguided Mode Around H^+ Gyrofrequency

For a given ion phase space density distribution $F(v_{||}, v_{\perp})$, the growth rate depends on the integration of the terms containing $\partial F(v_{||}, v_{\perp})/\partial v_{\perp}$ and $\partial F(v_{||}, v_{\perp})/\partial v_{||}$ along the resonant surface $v_{||} = (\omega - m\Omega_s)/k_{||}$. Based on Kennel et al. (Kennel, 1966), here, we derive a simplified form of the convective growth rate for the unguided mode near H^+ gyrofrequency to better demonstrate how the $F(v_{||}, v_{\perp})$ distribution leads to wave growth. In the environment of the radiation belt, the Stix parameter P dominates L , R and refractive index R_I . One can thus simplify the imaginary part of the first order of the dispersion function:

$$\begin{aligned} \text{Im } D^{(1)}(\omega, \mathbf{k}) &= -2\pi \sum_s \frac{\omega_{ps}^2}{\omega |k_{||}|} \int_0^\infty v_{\perp} dv_{\perp} \int_{-\infty}^{+\infty} dv_{||} \sum_m \delta \left(v_{||} - \frac{\omega - m\Omega_s}{k_{||}} \right) \\ &\quad \cdot 2Pv_{\perp} \left[R + L - 2R_I^2 \right] G_{ls}^*, \end{aligned} \quad (\text{B1})$$

where

$$G_{ls}^* \approx G_{ls} \frac{1}{2[R+L-2R_I^2]} \left[2(L-R_I^2)J_{m+1}^2 + 2(R-n^2)J_{m-1}^2 + R_I^2 \sin^2 \psi (J_{m+1} - J_{m-1})^2 \right] \\ = \left(\frac{\partial \bar{F}_s}{\partial v_\perp} - \frac{k_{||}}{\omega} \frac{\partial \bar{F}_s}{\partial \alpha} \right) \cdot \left[\frac{L-R_I^2}{R+L-2R_I^2} J_{m+1} + \frac{R-R_I^2}{R+L-2R_I^2} J_{m-1} \right]^2. \quad (\text{B2})$$

Following (Chen et al., 2010), express the magnitude of convective growth rate \mathbf{k}_i as

$$k_i = -\frac{\text{Im } D^{(1)}(\omega, \mathbf{k})}{\hat{\mathbf{k}} \cdot \partial D^{(0)}/\partial \mathbf{k}}, \quad (\text{B3})$$

here

$$\frac{\partial D^{(0)}}{\partial k} = \frac{8P}{k} [\cos^2 \psi R_I^4 - RL]. \quad (\text{B4})$$

Considering that the group velocity points in nearly the same direction as the wave vector for the unguided mode, one can finally express the component of \mathbf{k}_i in the group velocity direction as:

$$K_i = -\hat{\mathbf{k}} \cdot \hat{\mathbf{v}}_g k_i \\ \approx -k_i \\ \approx \frac{1}{2} \pi^2 \sum_s \frac{k \omega_{ps}^2}{|k_{||}| \omega} \frac{R+L-2R_I^2}{RL-\cos^2 \psi R_I^4} \int_0^\infty v_\perp^2 G_{ls}^* dv_\perp. \quad (\text{B5})$$

It can be proven that the product of the factors outside the integral is greater than zero, therefore, the values of G_{ls}^* represent the contribution to wave growth by hot ions with a given energy range.

Data Availability Statement

Data are available from the following websites: <http://emfisis.physics.uiowa.edu/Flight/>, <https://www.rbsp-ect.lanl.gov/>, <http://www.space.umn.edu/rbspefw-data/> and <http://rbspice.ftecs.com/Data.html>.

Acknowledgments

This work in China was supported by NSFC grants 41774171, 41974205, 41774167, 41804157, and 41904156. The authors also acknowledge the financial support provided by Shenzhen Science and Technology Research Program JCYJ20180306171918617 and Shenzhen Science and Technology Program (Group No. KQTD20180410161218820), and by Key Laboratory of Geospace Environment, Chinese Academy of Sciences, University of Science and Technology of China. Tielong Zhang was supported by CAS Center for Excellence in Comparative Planetology. The authors appreciate EMFISIS, ECT, EFW, and RSPICE teams for the use of Van Allen Probes data. Geng Wang thanks Zhenpeng Su, Xiongdong Yu, Xing Cao and Si Liu for helpful discussions.

References

- Allen, R. C., Zhang, J. C., Kistler, L. M., Spence, H. E., Lin, R. L., Dunlop, M. W., & André, M. (2013). Multiple bidirectional EMIC waves observed by Cluster at middle magnetic latitudes in the dayside magnetosphere. *Journal of Geophysical Research*, 118(10), 6266–6278. <https://doi.org/10.1002/jgra.50600>
- Allen, R. C., Zhang, J.-C., Kistler, L. M., Spence, H. E., Lin, R.-L., Klecker, B., et al. (2015). A statistical study of EMIC waves observed by Cluster: 1. Wave properties. *Journal of Geophysical Research: Space Physics*, 120, 5574–5592. <https://doi.org/10.1002/2015JA021333>
- Allen, R. C., Zhang, J. C., Kistler, L. M., Spence, H. E., Lin, R. L., Klecker, B., et al. (2016). A statistical study of EMIC waves observed by Cluster: 2. Associated plasma conditions. *Journal of Geophysical Research: Space Physics*, 121(7), 6458–6479. <https://doi.org/10.1002/2016JA022541>
- Anderson, B. J., & Hamilton, D. C. (1993). Electromagnetic ion cyclotron waves stimulated by modest magnetospheric compressions. *Journal of Geophysical Research*, 98, 11. <https://doi.org/10.1029/93JA00605>
- Bashir, M. F., & Ilie, R. (2018). A new N⁺ band of electromagnetic ion cyclotron waves in multi-ion cold plasmas. *Geophysical Research Letters*, 45(19), 10150–10159. <https://doi.org/10.1029/2018GL080280>
- Blum, L. W., Bonnell, J. W., Agapitov, O., Paulson, K., & Kletzing, C. (2017). EMIC wave scale size in the inner magnetosphere: Observations from the dual Van Allen Probes. *Geophysical Research Letters*, 44, 1227–1233. <https://doi.org/10.1002/2016GL072316>
- Blum, L. W., Halford, A., Millan, R., Bonnell, J. W., Goldstein, J., Usanova, M., et al. (2015). Observations of coincident EMIC wave activity and duskside energetic electron precipitation on 18–19 January 2013. *Geophysical Research Letters*, 42(14), 5727–5735. <https://doi.org/10.1002/2015GL065245>
- Blum, L. W., MacDonald, E. A., Gary, S. P., Thomsen, M. F., & Spence, H. E. (2009). Ion observations from geosynchronous orbit as a proxy for ion cyclotron wave growth during storm times. *Journal of Geophysical Research*, 114(A10), A10214. <https://doi.org/10.1029/2009JA014396>
- Bortnik, J., & Thorne, R. M. (2010). Transit time scattering of energetic electrons due to equatorially confined magnetosonic waves. *Journal of Geophysical Research*, 115, A07213. <https://doi.org/10.1029/2010JA015283>
- Cao, X., Ni, B., Summers, D., Bortnik, J., Tao, X., Shrubs, Y. Y., et al. (2017). Bounce resonance scattering of radiation belt electrons by N⁺ band EMIC waves. *Journal of Geophysical Research*, 122(2), 1702–1713. <https://doi.org/10.1002/2016JA023607>
- Chen, L., Thorne, R. M., & Horne, R. B. (2009). Simulation of EMIC wave excitation in a model magnetosphere including structured high-density plumes. *Journal of Geophysical Research*, 114, A07221. <https://doi.org/10.1029/2009JA014204>

- Chen, L., Thorne, R. M., Jordanova, V. K., & Horne, R. B. (2010). Global simulation of magnetosonic wave instability in the storm time magnetosphere. *Journal of Geophysical Research*, 115, A11222. <https://doi.org/10.1029/2010JA015707>
- Cornwall, J. M. (1965). Cyclotron instabilities and electromagnetic emission in the ultra low frequency and very low frequency ranges. *Journal of Geophysical Research*, 70(1), 61–69. <https://doi.org/10.1029/JZ070i001p00061>
- Daglis, I. A., Thorne, R. M., Baumjohann, W., & Orsini, S. (1999). The terrestrial ring current: Origin, formation, and decay. *Reviews of Geophysics*, 37, 407–438. <https://doi.org/10.1029/1999RG900009>
- Denton, R. E., Hudson, M. K., & Roth, I. (1992). Loss-cone-driven ion cyclotron waves in the magnetosphere. *Journal of Geophysical Research*, 97, 12. <https://doi.org/10.1029/92JA00954>
- de Soria-Santacruz, M., Spasovjevic, M., & Chen, L. (2013). EMIC waves growth and guiding in the presence of cold plasma density irregularities. *Geophysical Research Letters*, 40, 1940–1944. <https://doi.org/10.1002/grl.50484>
- Feygin, F., Nekrasov, A., Pikkarainen, T., Raita, T., & Prikner, K. (2007). Pc1 pearl waves with magnetosonic dispersion. *Journal of Atmospheric and Solar-Terrestrial Physics*, 69(14), 1644–1650. <https://doi.org/10.1016/j.jastp.2007.01.019>
- Fraser, B. J., & Nguyen, T. S. (2001). Is the plasmapause a preferred source region of electromagnetic ion cyclotron waves in the magnetosphere? *Journal of Atmospheric and Solar-Terrestrial Physics*, 63, 1225–1247. [https://doi.org/10.1016/S1364-6826\(00\)00225-X](https://doi.org/10.1016/S1364-6826(00)00225-X)
- Funsten, H. O., Skoug, R. M., Guthrie, A. A., MacDonald, E. A., Baldonado, J. R., Harper, R. W., et al. (2013). Helium, Oxygen, Proton, and Electron (HOPE) Mass Spectrometer for the Radiation Belt Storm Probes Mission. *Space Science Reviews*, 179, 423–484. <https://doi.org/10.1007/s11214-013-9968-7>
- Fuselier, S. A., Gary, S. P., Thomsen, M. F., Claflin, E. S., Hubert, B., Sandel, B. R., & Immel, T. (2004). Generation of transient dayside subauroral proton precipitation. *Journal of Geophysical Research*, 109(A12), A12227. <https://doi.org/10.1029/2004JA010393>
- Gamayunov, K. V., Min, K., Saikin, A. A., & Rassoul, H. (2018). Generation of EMIC waves observed by Van Allen Probes at low L shells. *Journal of Geophysical Research: Space Physics*, 123(10), 8533–8556. <https://doi.org/10.1029/2018JA025629>
- Gary, S. P. (1993). *Theory of space plasma microinstabilities*.
- Gary, S. P., & Lee, M. A. (1994). The ion cyclotron anisotropy instability and the inverse correlation between proton anisotropy and proton beta. *Journal of Geophysical Research*, 99(A6), 11297–11302. <https://doi.org/10.1029/94JA00253>
- Goldstein, J., Gallagher, D., Craven, P. D., Comfort, R. H., Genestreti, K. J., Mouikis, C., et al. (2019). Temperature dependence of plasmaspheric ion composition. *Journal of Geophysical Research: Space Physics*, 124(8), 6585–6595. <https://doi.org/10.1029/2019JA026822>
- Grison, B., Darrouzet, F., Santolík, O., Cornilleau-Wehrlin, N., & Masson, A. (2016). Cluster observations of reflected EMIC-triggered emission. *Geophysical Research Letters*, 43, 4164–4171. <https://doi.org/10.1002/2016GL069096>
- Halford, A. J., Fraser, B. J., & Morley, S. K. (2015). EMIC waves and plasmaspheric and plume density: CRRES results. *Journal of Geophysical Research*, 120, 1974–1992. <https://doi.org/10.1002/2014JA020338>
- Horne, R. B., & Thorne, R. M. (1993). On the preferred source location for the convective amplification of ion cyclotron waves. *Journal of Geophysical Research*, 98, 9233–9247. <https://doi.org/10.1029/92JA02972>
- Horne, R. B., & Thorne, R. M. (1994). Convective instabilities of electromagnetic ion cyclotron waves in the outer magnetosphere. *Journal of Geophysical Research*, 99, 17259. <https://doi.org/10.1029/94JA01259>
- Horne, R. B., & Thorne, R. M. (1997). Wave heating of he + by electromagnetic ion cyclotron waves in the magnetosphere' heating near the h+–he + bi-ion resonance frequency. *Journal of Geophysical Research*, 102(11), 11457–11471. <https://doi.org/10.1029/97JA00749>
- Hu, Y., & Denton, R. E. (2009). Two-dimensional hybrid code simulation of electromagnetic ion cyclotron waves in a dipole magnetic field. *Journal of Geophysical Research*, 114, A12217. <https://doi.org/10.1029/2009JA014570>
- Hu, Y., Denton, R. E., & Johnson, J. R. (2010). Two-dimensional hybrid code simulation of electromagnetic ion cyclotron waves of multi-ion plasmas in a dipole magnetic field. *Journal of Geophysical Research*, 115, A09218. <https://doi.org/10.1029/2009JA015158>
- Huba, J., & Krall, J. (2013). Modeling the plasmasphere with SAMI3. *Geophysical Research Letters*, 40(1), 6–10. <https://doi.org/10.1029/2012GL054300>
- Jun, C. W., Yue, C., Bortnik, J., Lyons, L. R., Nishimura, Y., & Kletzing, C. (2019). EMIC wave properties associated with and without injections in the inner magnetosphere. *Journal of Geophysical Research: Space Physics*, 124(3), 2029–2045. <https://doi.org/10.1029/2018JA026279>
- Kasahara, Y., Sawada, A., Yamamoto, M., Kimura, I., Kokubun, S., & Hayashi, K. (1992). Ion cyclotron emissions observed by the satellite Akebono in the vicinity of the magnetic equator. *Radio Science*, 27(2), 347–362. <https://doi.org/10.1029/91RS01872>
- Keika, K., Takahashi, K., Ukhorskiy, A. Y., & Miyoshi, Y. (2013). Global characteristics of electromagnetic ion cyclotron waves: Occurrence rate and its storm dependence. *Journal of Geophysical Research: Space Physics*, 118, 4135–4150. <https://doi.org/10.1002/jgra.50385>
- Kennel, C. (1966). Low-frequency whistler mode. *Physics of Fluids*, 9, 2190–2202. <https://doi.org/10.1063/1.1761588>
- Khazanov, G. V., Gamayunov, K. V., Gallagher, D. L., & Kozyra, J. U. (2006). Self-consistent model of magnetospheric ring current and propagating electromagnetic ion cyclotron waves: Waves in multi-ion magnetosphere. *Journal of Geophysical Research*, 111(A10), A10202. <https://doi.org/10.1029/2006JA011833>
- Khazanov, G. V., Gamayunov, K. V., Gallagher, D. L., & Kozyra, J. U. (2007). Reply to comment by R. M. Thorne and R. B. Horne on Khazanov et al. [2002] and Khazanov et al. [2006]. *Journal of Geophysical Research*, 112(A12), A12215. <https://doi.org/10.1029/2007JA012463>
- Kim, E.-H., & Johnson, J. R. (2016). Full-wave modeling of EMIC waves near the He + gyrofrequency. *Geophysical Research Letters*, 43(1), 13–21. <https://doi.org/10.1002/2015GL066978>
- Kistler, L. M., Mouikis, C. G., Spence, H. E., Menz, A. M., Skoug, R. M., Funsten, H. O., et al. (2016). The source of O + in the storm time ring current. *Journal of Geophysical Research*, 121(6), 5333–5349. <https://doi.org/10.1002/2015JA022204>
- Kletzing, C. A., Kurth, W. S., Acuna, M., MacDowall, R. J., Torbert, R. B., Averkamp, T., et al. (2013). The Electric and Magnetic Field Instrument Suite and Integrated Science (EMFISIS) on RBSP. *Space Science Reviews*, 179, 127–181. <https://doi.org/10.1007/s11214-013-9993-6>
- Kurth, W. S., De Pascuale, S., Faden, J. B., Kletzing, C. A., Hospodarsky, G. B., Thaller, S., & Wygant, J. R. (2015). Electron densities inferred from plasma wave spectra obtained by the Waves instrument on Van Allen Probes. *Journal of Geophysical Research: Space Physics*, 120, 904–914. <https://doi.org/10.1002/2014JA020857>
- Lee, D.-Y., Shin, D.-K., & Choi, C.-R. (2018). Effects of oblique wave normal angle and noncircular polarization of electromagnetic ion cyclotron waves on the pitch angle scattering of relativistic electrons. *Journal of Geophysical Research: Space Physics*, 123(6), 4556–4573. <https://doi.org/10.1029/2018JA025342>
- Lee, J. H., Turner, D. L., Vines, S. K., Allen, R. C., Toledo-Redondo, S., Bingham, S. T., et al. (2021). Application of cold and hot plasma composition measurements to investigate impacts on dusk-side electromagnetic ion cyclotron waves. *Journal of Geophysical Research: Space Physics*, 126(1), e2020JA028650. <https://doi.org/10.1029/2020JA028650>
- Liu, N., Su, Z., Zheng, H., Wang, Y., & Wang, S. (2018). Prompt disappearance and emergence of radiation belt magnetosonic waves induced by solar wind dynamic pressure variations. *Geophysical Research Letters*, 45, 585–594. <https://doi.org/10.1002/2017GL076382>

- Loto'Aniu, T. M., Fraser, B. J., & Waters, C. L. (2005). Propagation of electromagnetic ion cyclotron wave energy in the magnetosphere. *Journal of Geophysical Research*, 110, A07214. <https://doi.org/10.1029/2004JA010816>
- Mauk, B. H., Fox, N. J., Kanekal, S. G., Kessel, R. L., Sibeck, D. G., & Ukhorskiy, A. (2013). Science objectives and rationale for the Radiation Belt Storm Probes Mission. *Space Science Reviews*, 179, 3–27. <https://doi.org/10.1007/s11214-012-9908-y>
- Meredith, N. P., Horne, R. B., Kersten, T., Fraser, B. J., & Grew, R. S. (2014). Global morphology and spectral properties of EMIC waves derived from CRRES observations. *Journal of Geophysical Research: Space Physics*, 119, 5328–5342. <https://doi.org/10.1002/2014JA020064>
- Min, K., Lee, J., Keika, K., & Li, W. (2012). Global distribution of EMIC waves derived from THEMIS observations. *Journal of Geophysical Research*, 117, A05219. <https://doi.org/10.1029/2012JA017515>
- Min, K., Liu, K., Bonnell, J. W., Breneman, A. W., Denton, R. E., Funsten, H. O., et al. (2015). Study of EMIC wave excitation using direct ion measurements. *Journal of Geophysical Research: Space Physics*, 120, 2702–2719. <https://doi.org/10.1002/2014JA020717>
- Min, K., Takahashi, K., Ukhorskiy, A. Y., Manweiler, J. W., Spence, H. E., Singer, J., et al. (2017). Second harmonic poloidal waves observed by Van Allen Probes in the dusk-midnight sector. *Journal of Geophysical Research: Space Physics*, 122(3), 3013–3039. <https://doi.org/10.1002/2016JA023770>
- Mitchell, D. G., Lanzerotti, L. J., Kim, C. K., Stokes, M., Ho, G., Cooper, S., et al. (2013). Radiation Belt Storm Probes Ion Composition Experiment (RBSPICE). *Space Science Reviews*, 179(1–4), 263–308. <https://doi.org/10.1007/s11214-013-9965-x>
- Miyoshi, Y., Matsuda, S., Kurita, S., Nomura, K., Keika, K., Shoji, M., et al. (2019). EMIC waves converted from equatorial noise due to $M/Q = 2$ ions in the plasmasphere: Observations from Van Allen Probes and Arase. *Geophysical Research Letters*, 46. <https://doi.org/10.1029/2019GL083024>
- Miyoshi, Y., Sakaguchi, K., Shioikawa, K., Evans, D., Albert, J., Connors, M., & Jordanova, V. (2008). Precipitation of radiation belt electrons by EMIC waves, observed from ground and space. *Geophysical Research Letters*, 35, L23101. <https://doi.org/10.1029/2008GL035727>
- Ni, B., Cao, X., Zou, Z., Zhou, C., Gu, X., Bortnik, J., et al. (2015). Resonant scattering of outer zone relativistic electrons by multibeam and EMIC waves and resultant electron loss time scales. *Journal of Geophysical Research: Space Physics*, 120, 7357–7373. <https://doi.org/10.1002/2015JA021466>
- Omura, Y., Katoh, Y., & Summers, D. (2008). Theory and simulation of the generation of whistler-mode chorus. *Journal of Geophysical Research*, 113, A04223. <https://doi.org/10.1029/2007JA012622>
- Omura, Y., Pickett, J., Grison, B., Santolik, O., Dandouras, I., Engebretson, M., et al. (2010). Theory and observation of electromagnetic ion cyclotron triggered emissions in the magnetosphere. *Journal of Geophysical Research*, 115, A07234. <https://doi.org/10.1029/2010JA015300>
- Omura, Y., & Zhao, Q. (2013). Relativistic electron microbursts due to nonlinear pitch angle scattering by EMIC triggered emissions. *Journal of Geophysical Research: Space Physics*, 118(8), 5008–5020. <https://doi.org/10.1002/jgra.50477>
- Paulson, K. W., Smith, C. W., Lessard, M. R., Engebretson, M. J., Torbert, R. B., & Kletzing, C. A. (2014). In situ observations of Pc1 pearl pulsations by the Van Allen Probes. *Geophysical Research Letters*, 41(6), 1823–1829. <https://doi.org/10.1002/2013GL059187>
- Paulson, K. W., Smith, C. W., Lessard, M. R., Torbert, R. B., Kletzing, C. A., & Wygant, J. R. (2017). In situ statistical observations of Pc1 pearl pulsations and unstructured EMIC waves by the Van Allen Probes. *Journal of Geophysical Research: Space Physics*, 122(1), 105–119. <https://doi.org/10.1002/2016JA023160>
- Rauch, J. L., & Roux, A. (1982). Ray tracing of ULF waves in a multicomponent magnetospheric plasma—Consequences for the generation mechanism of ion cyclotron waves. *Journal of Geophysical Research*, 87, 8191–8198. <https://doi.org/10.1029/JA087A10p08191>
- Rodger, C. J., Hendry, A. T., Clilverd, M. A., Kletzing, C. A., Brundell, J. B., & Reeves, G. D. (2015). High-resolution in situ observations of electron precipitation-causing EMIC waves. *Geophysical Research Letters*, 42, 9633–9641. <https://doi.org/10.1002/2015GL066581>
- Saikin, A. A., Jordanova, V. K., Zhang, J. C., Smith, C. W., Spence, H. E., Larsen, B. A., et al. (2018). Comparing simulated and observed EMIC wave amplitudes using in situ Van Allen Probes' measurements. *Journal of Atmospheric and Solar-Terrestrial Physics*, 177, 190–201. <https://doi.org/10.1016/j.jastp.2018.01.024>
- Saikin, A. A., Zhang, J.-C., Allen, R. C., Smith, C. W., Kistler, L. M., Spence, H. E., et al. (2015). The occurrence and wave properties of H^+ -, He^{+} -, and O^{+} -band EMIC waves observed by the Van Allen Probes. *Journal of Geophysical Research: Space Physics*, 120, 7477–7492. <https://doi.org/10.1002/2015JA021358>
- Santolík, O., Parrot, M., & Lefevre, F. (2003). Singular value decomposition methods for wave propagation analysis. *Radio Science*, 38, 1010. <https://doi.org/10.1029/2000RS002523>
- Santolík, O., Pickett, J. S., Gurnett, D. A., Menietti, J. D., Tsurutani, B. T., & Verkhoglyadova, O. (2010). Survey of Poynting flux of whistler mode chorus in the outer zone. *Journal of Geophysical Research*, 115, A00F13. <https://doi.org/10.1029/2009JA014925>
- Smith, R. L., & Brice, N. (1964). Propagation in multicomponent plasmas. *Journal of Geophysical Research*, 69(23), 5029–5040. <https://doi.org/10.1029/JZ069i023p05029>
- Stix, T. H. (1992). *Waves in plasmas*. New York: American Institute of Physics.
- Su, Z., Gao, Z., Zheng, H., Wang, Y., Wang, S., Spence, H. E., et al. (2017). Rapid loss of radiation belt relativistic electrons by EMIC waves. *Journal of Geophysical Research: Space Physics*, 122, 9880–9897. <https://doi.org/10.1002/2017JA024169>
- Su, Z., Zhu, H., Xiao, F., Zheng, H., Zhang, M., Liu, Y.-M., et al. (2014). Latitudinal dependence of nonlinear interaction between electromagnetic ion cyclotron wave and terrestrial ring current ions. *Physics of Plasmas*, 21(5), 052310. <https://doi.org/10.1063/1.4880036>
- Takahashi, K., Denton, R. E., Anderson, R. R., & Hughes, W. J. (2006). Mass density inferred from toroidal wave frequencies and its comparison to electron density. *Journal of Geophysical Research*, 111, A01201. <https://doi.org/10.1029/2005JA011286>
- Tao, X., & Bortnik, J. (2010). Nonlinear interactions between relativistic radiation belt electrons and oblique whistler mode waves. *Nonlinear Processes in Geophysics*, 17, 599–604. <https://doi.org/10.5194/npg-17-599-2010>
- Terrick, S. S., Engebretson, M. J., Posch, J. L., Olson, C. N., Smith, C. W., Denton, R. E., et al. (2017). Location of intense electromagnetic ion cyclotron (EMIC) wave events relative to the plasmapause: Van Allen Probes observations. *Journal of Geophysical Research: Space Physics*, 122, 4064–4088. <https://doi.org/10.1002/2016JA023392>
- Thorne, R. M., & Horne, R. B. (1992). The contribution of ion-cyclotron waves to electron heating and SAR-arc excitation near the storm-time plasmapause. *Geophysical Research Letters*, 19, 417–420. <https://doi.org/10.1029/92GL00089>
- Thorne, R. M., & Horne, R. B. (1993). Cyclotron absorption of ion-cyclotron waves at the bi-ion frequency. *Geophysical Research Letters*, 20, 317–320. <https://doi.org/10.1029/93GL00089>
- Thorne, R. M., & Horne, R. B. (2007). Comment on Khazanov et al. [2002] and Khazanov et al. [2006]. *Journal of Geophysical Research*, 112(A12), A12214. <https://doi.org/10.1029/2007JA012268>
- Thorne, R. M., Horne, R. B., Jordanova, V. K., Bortnik, J., & Glauert, S. (2006). Interaction of EMIC waves with thermal plasma and radiation belt particles. In K. Takahashi, P. J. Chi, R. E. Denton, & R. L. Lysak (Eds.), *Magnetospheric ULF waves: Synthesis and new directions* (Vol. 169, pp. 213–223). <https://doi.org/10.1029/169GM14>

- Usanova, M. E., Drozdov, A., Orlova, K., Mann, I. R., Shprits, Y., Robertson, M. T., et al. (2014). Effect of EMIC waves on relativistic and ultrarelativistic electron populations: Ground-based and Van Allen Probes observations. *Geophysical Research Letters*, 41, 1375–1381. <https://doi.org/10.1002/2013GL059024>
- Vines, S. K., Allen, R. C., Anderson, B. J., Engebretson, M. J., Fuselier, S. A., Russell, C. T., et al. (2019). EMIC waves in the outer magnetosphere: Observations of an off-Equator source region. *Geophysical Research Letters*, 46(11), 5707–5716. <https://doi.org/10.1029/2019GL082152>
- Wang, D., Yuan, Z., Yu, X., Deng, X., Zhou, M., Huang, S., et al. (2015). Statistical characteristics of EMIC waves: Van Allen Probe observations. *Journal of Geophysical Research: Space Physics*, 120, 4400–4408. <https://doi.org/10.1002/2015JA021089>
- Wang, G., Su, Z., Zheng, H., Wang, Y., Zhang, M., & Wang, S. (2017). Nonlinear fundamental and harmonic cyclotron resonant scattering of radiation belt ultrarelativistic electrons by oblique monochromatic EMIC waves. *Journal of Geophysical Research: Space Physics*, 122, 1928–1945. <https://doi.org/10.1002/2016JA023451>
- Wang, G., Zhang, T. L., Gao, Z. L., Wu, M. Y., Wang, G. Q., & Schmid, D. (2019). Propagation of EMIC waves inside the plasmasphere: A two-event study. *Journal of Geophysical Research: Space Physics*, 124(11), 8396–8415. <https://doi.org/10.1029/2019JA027055>
- Wang, X. Y., Huang, S. Y., Allen, R. C., Fu, H. S., Deng, X. H., Zhou, M., et al. (2017). The occurrence and wave properties of EMIC waves observed by the Magnetospheric Multiscale (MMS) mission. *Journal of Geophysical Research: Space Physics*, 122(8), 8228–8240. <https://doi.org/10.1002/2017JA024237>
- Wang, Z., Yuan, Z., Li, M., Li, H., Wang, D., Li, H., et al. (2014). Statistical characteristics of EMIC wave-driven relativistic electron precipitation with observations of POES satellites: Revisit. *Journal of Geophysical Research*, 119, 5509–5519. <https://doi.org/10.1002/2014JA020082>
- Yu, X., & Yuan, Z. (2019). Saturation characteristics of parallel EMIC waves in the inner magnetosphere. *Geophysical Research Letters*, 46(14), 7902–7910. <https://doi.org/10.1029/2019GL083630>
- Yu, X., Yuan, Z., Wang, D., Huang, S., Qiao, Z., Yu, T., & Yao, F. (2016). Excitation of oblique O⁺ band EMIC waves in the inner magnetosphere driven by hot H⁺ with ring velocity distributions. *Journal of Geophysical Research: Space Physics*, 121, 11. <https://doi.org/10.1002/2016JA023221>
- Yuan, Z., Xiong, Y., Huang, S., Deng, X., Pang, Y., Zhou, M., et al. (2014). Cold electron heating by EMIC waves in the plasmaspheric plume with observations of the Cluster satellite. *Geophysical Research Letters*, 41, 1830–1837. <https://doi.org/10.1002/2014GL059241>
- Yuan, Z., Yu, X., Ouyang, Z., Yao, F., Huang, S., & Funsten, H. O. (2019). Simultaneous trapping of EMIC and MS waves by background plasmas. *Journal of Geophysical Research: Space Physics*, 124, 1635–1643. <https://doi.org/10.1029/2018JA026149>
- Yue, C., Jun, C.-W., Bortnik, J., An, X., Ma, Q., Reeves, G. D., et al. (2019). The relationship between EMIC wave properties and proton distributions based on Van Allen Probes observations. *Geophysical Research Letters*, 46(8), 4070–4078. <https://doi.org/10.1029/2019GL082633>
- Zhang, J.-C., Saikin, A. A., Kistler, L. M., Smith, C. W., Spence, H. E., Mouikis, C. G., et al. (2014). Excitation of EMIC waves detected by the Van Allen Probes on 28 April 2013. *Geophysical Research Letters*, 41, 4101–4108. <https://doi.org/10.1002/2014GL060621>
- Zhang, X. J., Li, W., Thorne, R. M., Angelopoulos, V., Ma, Q., Li, J., et al. (2016). Physical mechanism causing rapid changes in ultrarelativistic electron pitch angle distributions right after a shock arrival: Evaluation of an electron dropout event. *Journal of Geophysical Research: Space Physics*, 121(9), 8300–8316. <https://doi.org/10.1002/2016JA022517>
- Zhao, H., Li, X., Baker, D. N., Fennell, J. F., Blake, J. B., Larsen, B. A., et al. (2015). The evolution of ring current ion energy density and energy content during geomagnetic storms based on Van Allen Probes measurements. *Journal of Geophysical Research: Space Physics*, 120(9), 7493–7511. <https://doi.org/10.1002/2015JA021533>
- Zhu, H., Chen, L., Claudepierre, S. G., & Zheng, L. (2020). Direct evidence of the pitch angle scattering of relativistic electrons induced by EMIC waves. *Geophysical Research Letters*, 47(4), e2019GL085637. <https://doi.org/10.1029/2019GL085637>